Mon. Not. R. Astron. Soc. **000**, 000–000 (0000) Printed 8 March 2017 (MN LATEX style file v2.2)

SCUBA-2 follow-up of *Herschel*-SPIRE observed *Planck* overdensities

Todd P. MacKenzie[1], Douglas Scott[1], Matteo Bianconi[2], David L. Clements[3], Herve A. Dole[4], I. Flores-Cacho[5,6], David Guery[4], R. Kneissl[7,8], G. Lagache[9], Francine R. Marleau[2], L. Montier[5,6], N. P. H. Nesvadba[4], Etienne Pointecouteau[5,6], G. Soucail[5,6]

[1] *Department of Physics & Astronomy, University of British Columbia, 6224 Agricultural Road, Vancouver, BC V6T 1Z1, Canada*
[2] *Institute of Astro and Particle Physics, University of Innsbruck, 6020 Innsbruck, Austria*
[3] *Physics Department, Blackett Lab, Prince Consort Road, London SW7 2AZ, UK*
[4] *Institut d'Astrophysique Spatiale, Univ. Paris-Sud & CNRS, Univ. Paris-Saclay - IAS, bâtiment 121, univ Paris-Sud, 91405 Orsay, France*
[5] *Université de Toulouse, UPS-OMP, IRAP, 31028, Toulouse Cedex 4, France*
[6] *CNRS, IRAP, 9 Av. Colonel Roche, BP 44346, 31028, Toulouse Cedex 4, France*
[7] *Atacama Large Millimeter/submillimeter Array, ALMA Santiago Central Offices, Alonso de Cordova 3107, Vitacura, Casilla 763 0355, Santiago, Chile*
[8] *European Southern Observatory, ESO Vitacura, Alonso de Cordova 3107, Vitacura, Casilla 19001, Santiago, Chile*
[9] *Aix Marseille Université, CNRS, LAM (Laboratoire d'Astrophysique de Marseille) UMR 7326, 13388, Marseille, France*

arXiv:1703.02074v1 [astro-ph.GA] 6 Mar 2017

8 March 2017

ABSTRACT

We present SCUBA-2 follow-up of 61 candidate high-redshift *Planck* sources. Of these, 10 are confirmed strong gravitational lenses and comprise some of the brightest such submm sources on the observed sky, while 51 are candidate proto-cluster fields undergoing massive starburst events. With the accompanying *Herschel*-SPIRE observations and assuming an empirical dust temperature prior of 34^{+13}_{-9} K, we provide photometric redshift and far-IR luminosity estimates for 172 SCUBA-2-selected sources within these *Planck* overdensity fields. The redshift distribution of the sources peak between a redshift of 2 and 4, with one third of the sources having $S_{500}/S_{350} > 1$. For the majority of the sources, we find far-IR luminosities of approximately $10^{13}\,\mathrm{L}_{\odot}$, corresponding to star-formation rates of around $1000\,\mathrm{M}_{\odot}\mathrm{yr}^{-1}$. For $S_{850} > 8$ mJy sources, we show that there is up to an order of magnitude increase in star-formation rate density and an increase in uncorrected number counts of 6 for $S_{850} > 8$ mJy when compared to typical cosmological survey fields. The sources detected with SCUBA-2 account for only approximately 5 per cent of the *Planck* flux at 353 GHz, and thus many more fainter sources are expected in these fields.

Key words: galaxies: clusters: general – submillimetre: galaxies

1 INTRODUCTION

Modern submm observatories, such as the JCMT (Holland et al. 1999), BLAST(Pascale et al. 2008) and *Herschel* (Pilbratt et al. 2010), have allowed us to view larger and larger portions of the submm sky to greater and greater depths, continually improving the statistics on this relatively new population of sources. Of particular interest is the role of such sources in the census of global star-formation rates (SFRs) and understanding the driving force behind their intense star-formation activity. While some may be triggered by mergers (e.g. Clements et al. 1996; Murphy et al. 1996; Sanders & Mirabel 1996), others may simply be at the bright end of what has been named the "main sequence" of galaxies (Noeske et al. 2007; Daddi et al. 2007; Elbaz et al. 2011). Most wide-field cosmology surveys try to characterise this population as a whole, but it is important to consider the effects of galaxy environment on star-formation. Due to detection techniques, most known clusters are at redshifts below that of the peak of global star-formation, and the star-formation rate of cluster members has been quenched through various physical processes, although

galaxies falling into their gravitational potential wells for the first time may still experience an increase in star-formation (Verdugo et al. 2008; Braglia et al. 2009, 2011). The Sunyaev-Zeldovich effect, providing largely redshift-independent selection, has been used to detect hundreds of clusters out to $z \sim 1.5$ (e.g. Planck Collaboration VIII 2011; Hasselfield et al. 2013; Planck Collaboration XXIX 2014; Planck Collaboration XX 2014; Bleem et al. 2015). Similarily, the Spitzer Infrared Array Camera (IRAC) Shallow Survey used 4.5 μm selected sources and photometric redshifts to identify over a hundred candidate clusters with redshifts ranging from 1 to 1.7 (Eisenhardt et al. 2008).

A complementary high-z cluster detection technique is to look for regions of exceptional star-formation. Due to the density of such objects on the sky, large areas must be probed in order to find a significant sample, thus all-sky surveys are needed. *Planck* (with its 5 arcminute beam that closely matches the expected size of a forming galaxy cluster at $z \sim 2$–4), along with its all-sky coverage, is an excellent observatory for finding such objects. Indeed, followup of objects already observed by *Herschel* from the *Planck* Early Release Compact Source Catalog (Planck Collaboration VII 2011) revealed four star-forming clusters out to a redshift of 2.3 (Clements et al. 2014). However, the area mapped by *Herschel* is only about 90 deg^2, and thus there remains a much larger portion of the sky that is mapped by *Planck*, but not *Herschel*. The search for further star-forming cluster candidates not yet observed by *Herschel* has already been performed and the first results can be found in Planck Collaboration XXXIX (2015). The catalogue contains 2151 objects comprising the *Planck* high-z (PHZ) catalogue found using 26 per cent of the sky.

Two methods were used to generate a list of potential high-z targets to follow-up with *Herschel* (see Planck Collaboration XXVII 2015 for details). The first of the two methods is explicitly detailed in Planck Collaboration XXXIX (2015), leading to the PHZ list, which will be available on the Planck Legacy Archive. This method uses Cosmic Microwave Background (CMB) and Galactic-cirrus-cleaned *Planck* maps at 353, 545 and 857 GHz, using the 26 per cent of the sky that is the least contaminated by Galactic sources. S/N $>$ 5 sources were identified in a 545 GHz "excess" map, defined to be the 545 GHz map with a linear interpolation between the 353 and 857 GHz maps subtracted. On top of this, S/N $>$ 3 detections were required at 353, 545 and 857 GHz. To remove cold Galactic cores and extragalactic radio sources, only detections with $S_{545}/S_{857} > 0.5$ and $S_{353}/S_{545} < 0.9$ were retained. The second method used the Planck Catalogue of Compact Sources (PCCS, Planck Collaboration XXVIII 2014) and a selection method based on the work of Negrello et al. (2010). Here, 52 per cent of the sky was used, based on the 857 GHz Galactic mask, and sources with S/N $>$ 4 at 545 GHz were selected from the catalogue. From this list, sources were only retained with $S_{857}/S_{545} < 1.5$ and $S_{217}/S_{353} < 1$, and which were not identified as a local galaxy, a bright radio source or Galactic cirrus in either the NASA/IPAC Extragalactic Database (NED), ALADIN, or *IRAS* maps. The result is a list of high-z candidate sources, selected to have apparent redshifted flux densities peaking between 353 and 857 GHz. Included in this is a combination of strongly lensed sources, proto-clusters undergoing massive starbursts, chance overdensities of star forming galaxies, and perhaps a few Galactic interlopers. The fraction of objects in the various categories is currently unknown, which is why follow-up observations are critical.

A total of 228 of these candidates were observed by *Herschel* using the Spectral and Photometric Imaging Receiver (SPIRE, Griffin et al. 2010). This instrument, with a beamsize 16 times smaller than *Planck*'s, has the ability to resolve the *Planck* candidates into either single bright point sources or many fainter sources. The former were shown by Canameras et al. (2015) to be among the brightest strongly lensed sources on the sky; 11 out of 15 of these bright sources were followed-up (two more were previously known, as discussed in Fu et al. 2012 and Combes et al. 2012, while the remaining two are in the far south) with a host of instruments, including SCUBA-2 at 850 μm, spectroscopic observations using the wide-band heterodyne receiver Eight MIxer Receiver (EMIR) at the Institut de Radioastronomie Millimétrique telescope (IRAM) and SMA 850 μm interferometry, to confirm their lensed nature. Their redshifts range from 2.2 to 3.6, with peak flux densities from 0.35 to 1.14 Jy, and they have apparent far-IR luminosities up to 3×10^{14} L$_\odot$. Due to their extra-ordinary flux densities and far-IR luminosities, these sources have been named "*Planck*'s dusty GEMS" (Gravitationally Enhanced subMillimetre Sources).

The first results covering the other class of source, namely the "overdensity fields," are presented in Planck Collaboration XXVII (2015). Significant enhancements in the surface density of sources were found at 350 and 500 μm, with the majority of sources peaking at 350 μm. Assuming an average dust temperature of 35 K, Planck Collaboration XXVII (2015) found a typical redshift of 2 for the overdensity fields, with average far-IR luminosities of around 4×10^{12} L$_\odot$ per SPIRE source. These *Planck*-selected sources may be high redshift proto-clusters undergoing rapid starformation, although some may also be chance line-of-sight alignments. Without spectroscopic redshift estimates of the objects within these overdensities, it is impossible to distinguish between these two possibilities.

The analysis here focuses on the SCUBA-2 observations, based on 61 of the 228 *Herschel* fields, which have been followed up with 850 μm observations at the JCMT. 10 of these fields are observations of *Planck*'s dusty GEMS and are detailed in Canameras et al. (2015). The 51 "overdensity fields" are discussed here. The more favourable "k-correction" (Franceschini et al. 1991; Blain & Longair 1993) at 850 μm means that we have a significantly less biased view of the redshift distribution of the overdensity fields than *Herschel*-SPIRE, and a greater sensitivity to sources at redshifts $\gtrsim 3$. We use the SEDeblend method adapted from MacKenzie et al. (2014), as described in more detail in MacKenzie et al. (2015), to fit modified blackbody SEDs to the SCUBA-2-detected sources. This method deblends SEDs directly from the maps, as opposed to a traditional approach where flux densities are deblended first, followed by subsequent SED fitting to the deblended fluxes. Degeneracy information between neighbouring confused sources is therefore retained, which is reflected in the fit parameters constraints, and more robustly deals with the confused nature of the *Herschel*-SPIRE imaging. To do this, we use the SCUBA-2 positions and fluxes, as well as the *Herschel*-SPIRE imaging. We use a relatively weak prior on dust temperature to break

its degeneracy with redshift, giving us useful constraints on both redshift and far-IR luminosity. Throughout we employ a ΛCDM cosmology with $\Omega_\Lambda = 0.692$, $\Omega_\mathrm{m} = 0.308$, and $H_0 = 67.8\,\mathrm{km\,s^{-1}\,Mpc^{-1}}$ (Planck Collaboration XIII 2015).

2 THE PLANCK CANDIDATES FOLLOW-UP

2.1 SCUBA-2 follow-up

51 overdensity fields observed with *Herschel*-SPIRE have been followed-up with SCUBA-2 850 μm observations at the JCMT (project codes M12AC19, M13AC22, M13BC05, M13BU09 and M14AC02) with approximately 10 arcminute diameter "daisy" scans. The initial observation strategy involved 20 minute scans repeated twice in grade 3 weather, while later observations used 30 minute scans repeated three times in grade 2 and 3 weather. The observations were reduced using SMURF (Chapin et al. 2013) called from the ORAC-DR pipeline (Gibb & Jenness 2010) using the standard blank-field map-making recipe optimised for finding point-sources. Readings from the JCMT water-vapour monitor (WVM, Dempsey & Friberg 2008) and the scaling relations found by Dempsey et al. (2010) were used to correct for atmospheric extinction.

To facilitate finding and extracting point-sources, we use the standard "matched-filter" provided by ORAC-DR. This procedure subtracts a 30 arcsecond smoothed map from a map convolved with the point spread function of the telescope and applying a correction factor such that point sources return the expected flux density. This correction factor accounts for source attenuation by both matched-filtering and bolometer time-series high-pass filtering by SMURF, and is estimated by injecting simulated sources into bolometer time-series and recovering their flux density after map-making, matched-filtering and source extraction. The minimum rms depths of each field range from 1.5 to 3 mJy (instrumental noise), with a median of 1.9 mJy for point sources in the matched-filtered images. We extract peak flux densities and positions from these maps to generate a catalogue of 172 SCUBA-2-detected sources with $\mathrm{S/N} > 4$ in $1.20\,\mathrm{deg}^2$ of sky for the 51 *Planck* overdensity fields. Fig. 1 shows SCUBA-2 positions plotted over the 350 μm Herschel SPIRE images for six fields with the densest concentration of SCUBA-2 sources. We also require a flux density uncertainty of less than 4 mJy for every source, since higher noise regions near the edges of the maps are more likely to contain artefacts of the map-making procedure. Of the $1.2\,\mathrm{deg}^2$, $0.69\,\mathrm{deg}^2$ was within the *Planck* beams, which we define to be the area in the *Planck* 353 GHz map with flux density greater than half the peak flux density of the *Planck* source, as in Planck Collaboration XXVII (2015). Of the 172 SCUBA-2-detected sources, 138 are located within the *Planck* beam. Table 1 list the source positions and flux densities, as well as constraints on their far-IR luminosities and redshifts. We refrain from deboosting the flux densities of our catalogue since the number counts in these regions will differ from those in cosmological fields, and hence it is hard to estimate the effects of confusion (see e.g. Coppin et al. 2006; Scott et al. 2010).

In order to asses the number of spurious sources within our catalogue, we perform the same source extraction procedure described above to search for negative sources within our maps. For this process, we avoid negative sources associated with "negative bowls" surrounding bright positive sources caused by the matched-filter. We find a total of 28 negative sources that satisfy our search criteria, which is higher than the roughly 2 expected spurious sources given the area observed and chosen signal-to-noise threshold. However, if we consider the effects of confusion noise of about 0.7 mJy per beam, the number of spurious negative sources with $\mathrm{S/N} > 4$ is reduced to 15. We believe this excess of significantly negative sources is the result of relatively few repeats of the observation fields and resulting map-making artefacts. Because the probability of detecting both false negatives and false positives should be equal, we expect an equal number of false positives in our catalogue. By characterising the properties of the false negative sources, we can correct for the false positive contributions when estimating the redshift distribution and global co-moving star-formation density of the sources in our catalogue. More information about these false negatives and their properties is given below.

2.2 *Herschel*-SPIRE data

All our observed fields have accompanying *Herschel*-SPIRE observations at 250, 350 and 500 μm. These observations have been reduced using HIPE 10 (Ott 2010), with the details given in Planck Collaboration XXVII (2015). The images have instrumental noise levels of 7.7, 6.3 and 7.6 mJy per pixel using the standard pixel sizes of 6, 10 and 14 arcseconds at 250, 350 and 500 μm, respectively. Thus, the noise levels in the images are near the confusion limit of *Herschel*-SPIRE (Nguyen et al. 2010), which we estimate to be 7.4, 8.7 and 8.6 at 250, 350 and 500 μm, respectively for our fields. Confusion noise is the result having an average of more than one source per beam, creating an undulating background. This limits the precision to which you can know the flux density of a source in the observations and the quoted values are one sigma uncertainties.

3 SED MODEL AND FITTING

We use the SEDeblend method as described in MacKenzie et al. (2015) to constrain SED parameters for each source. This method forward-models every source SED into the image plane to reconstruct simulated observations at each wavelength simultaneously. This model is then fit using Monte Carlo Markov chain (MCMC) Metropolis-Hastings algorithm (Metropolis et al. 1953; Hastings 1970) and uses a likelihood calculation that accounts for the effects of confusion noise in the *Herschel*-SPIRE observations. The version of SEDeblend applied here has a few key differences. First, since we do not have a catalogue of nearby sources to use for deblending, we instead use blank sky data to estimate the sky covariance matrix. Specifically, we turn to the GOODS-North HerMES field used in MacKenzie et al. (2014), with Gaussian random noise added in quadrature to the instrumental noise, so that the images contain the same noise levels as the *Planck* overdensity fields. While the confusion noise in our fields will be higher than that of a blank field, we estimate that the total per pixel noise in our fields is only 10 to 15% higher than blank fields

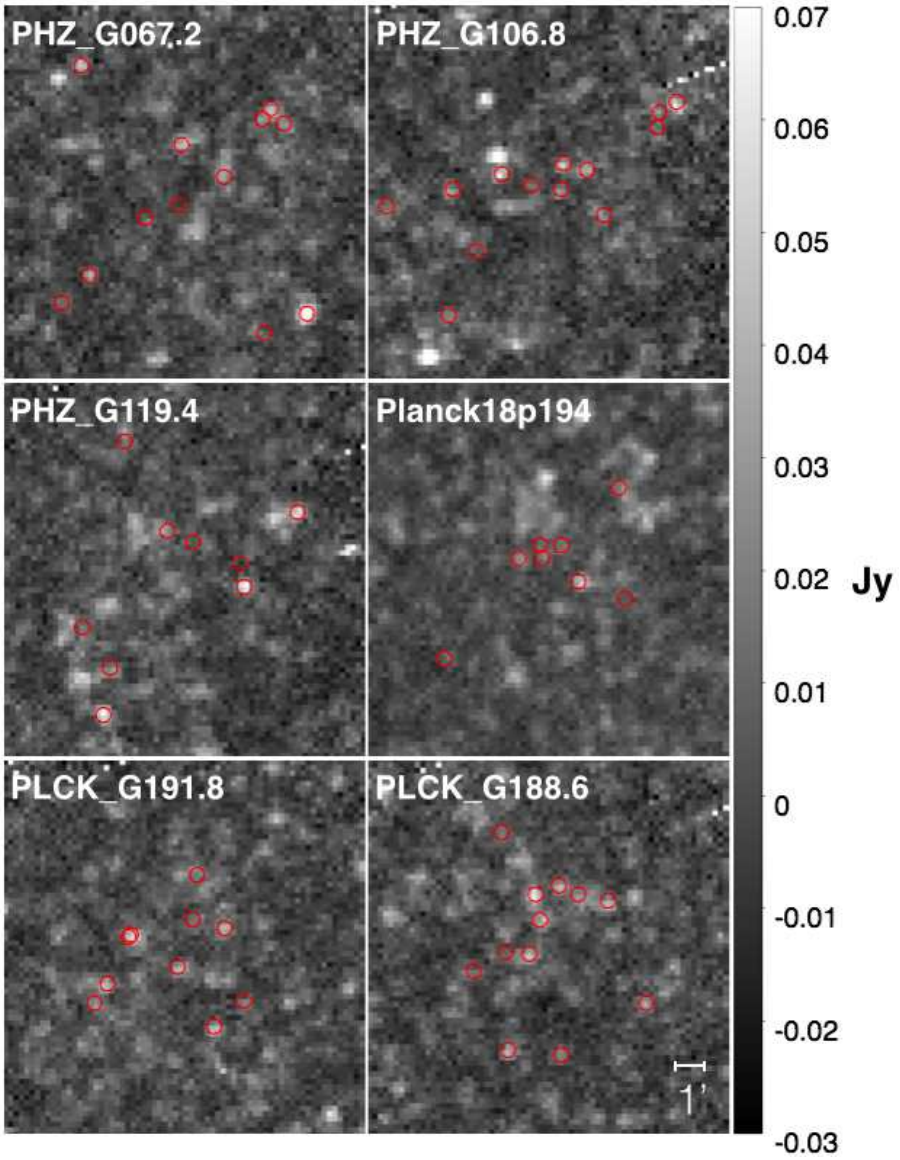


Figure 1. SCUBA-2 850 μm positions (red circles) plotted on the 350 μm *Herschel* SPIRE images for the six fields with the densest concentration of SCUBA-2 sources. For the majority of the sources, we find far-IR luminosities of approximately 10^{13} $L_{\odot}$, corresponding to star-formation rates of around 1000 $M_{\odot}yr^{-1}$. For $S_{850} > 8$ mJy sources, we show that there is up to an order of magnitude increase in star-formation rate density and an increase in uncorrected number counts of approximately 6 for $S_{850} > 8$ mJy when compared to typical cosmological survey fields.

observed for the same amount of time. We treat the SCUBA-2-detected sources in the same way as the ALMA-resolved LESS sources in MacKenzie et al. (2015), using the source positions and flux density estimates at 850 μm (although source positions are not as well constrained, of course). To account for source position uncertainty, we allow source positions to vary, with a 3 arcsecond positional prior, applied to the radial offset, up to a maximum of 10 arcseconds. Such positional errors are typical for 5σ SCUBA-2 850 μm sources (e.g. Simpson et al. 2015). In addition to allowing for source position uncertainties, we allow the telescope pointing to vary with a 1.5 arcsecond prior. The former positional prior accounts for source position uncertainty due to instrumental noise and applies to sources individually, while the latter accounts for telescope pointing uncertainty and affects all sources within a field in the same manner. An additional 5 per cent calibration uncertainty is applied to the SCUBA-2 flux estimates (Dempsey et al. 2013). Far-IR luminosities are calculated by integrating the model SED from 8 to 1000 μm.

While the ALMA LABOCA ECDFS Submm Survey (ALESS) sample had independent photometric redshift estimates (Simpson et al. 2014), our catalogue does not. Instead, we apply a prior on dust temperature in order to generate estimates for both redshifts and far-IR luminosities of our sample. Of course, redshift estimates would change if we used a different dust temperature prior; however, we make sure to choose a prior distribution with a realistic width,

and to the extent that the dust temperature does not change dramatically with redshift, our far-IR luminosity estimates should be reasonably accurate. Using sources above the 4.2 mJy flux density limit of the LABOCA ECDFS Submm Survey (LESS) for the ALESS follow-up in MacKenzie et al. (2015), we find a dust temperature distribution of 34^{+13}_{-9} K (using the 16th, 50th and 84th per centile values), and we adopt this fairly broad distribution as our dust temperature prior. Note that this represents the width of the distribution and not the error on the mean of the distribution. This central dust temperature and range of this prior is consistent with previous estimates for sources selected at 850 μm (e.g. Chapman et al. 2005; Swinbank et al. 2014).

In addition to fitting SEDs to the SCUBA-2-selected sources in the *Planck* overdensity fields, we apply the same method to SCUBA-2-selected sources from the Cosmology Legacy Survey (CLS, Simpson et al. 2015) within the Ultra Deep Survey (UDS) field (Lawrence et al. 2007). This field also has accompanying *Herschel*-SPIRE observations from HerMES (Oliver et al. 2012). By performing an identical analysis on the sources that are detected in this field, we are able to perform a direct comparison with the *Planck* overdensity fields. In addition to the availability of both SCUBA-2 and *Herschel*-SPIRE observations, this field was chosen because the data are deeper and the area of the sky surveyed is almost identical to that covered by the *Planck* overdensity fields. Before fitting SEDs to these sources, we add Gaussian random noise in quadrature to the instrumental noise of the HerMES SPIRE images to give it the same noise levels as the *Planck* overdensity fields, while accounting for the difference in pixel sizes. This catalogue contains 619 SCUBA-2-detected sources within 1.05 deg^2 of sky, with an average source flux density uncertainty of 1.2 mJy. The large number of sources found in this field is due to the longer integration time and steep submm number counts. Similarily, we find 26 negative sources within the UDS field.

4 SED FITTING RESULTS

The results of the SED fitting are shown in Fig. 2 and listed in Table 1 along with 68 per cent confidence intervals. Due to the wavelength coverage of the data, we are not able to constrain redshifts for sources with redshifts greater than about 6.5, and for those sources we report the 16th per centile of the distributions as a 1σ lower confidence limit. For high redshift sources, these limits are affected by a hard prior that sources cannot have a redshift greater than 10. Using our temperature prior of 34^{+13}_{-9} K, we achieve a photometric redshift uncertainty of $\delta z/(1+z) \approx 0.28$, with 68 per cent confidence intervals skewed to higher redshifts due to the asymmetric prior. In addition to fitting SEDs to the 172 SCUBA-2-detected sources, we perform a further test of our method by fitting SEDs to the 28 negative sources in the map above the 4σ cutoff (treating the negative flux densities at 850 μm as positive). Since there should be no *Herschel* counterparts, the majority of these sources are constrained to the high redshift region of Fig. 2, with 19 of the 28 negative sources falling into this category. Of the 172 positive sources in our catalogue, 32 sources have median redshifts greater than 6.5, and should be considered suspect. Only nine negative sources coincidentally have *Herschel* counterparts and redshift estimates lower than 6.5; this lack of spurious sources with low inferred reshifts suggests that sources with lower redshifts should be considered more reliable (approximately 6 per cent contamination).

5 DISCUSSION

In Fig. 2, the majority of well-constrained sources have far-IR luminosity estimates of around 10^{13}L$_\odot$, corresponding to SFRs of roughly 1000 M$_\odot$ yr^{-1}. On average, these sources are more luminous than those found in Planck Collaboration XXVII (2015), which have an average of 4×10^{12}L$_\odot$ (assuming a dust temperature of 35 K), although this is easily explained when considering the selection effects. A representative 2 mJy 1σ detection limit at 850 μm for a 34 K source is plotted in Fig. 2 with a solid blue line, along with *Herschel*-SPIRE confusion limits for a source of the same dust temperature and dust emissivity. From these detection limits, it is clear that SCUBA-2 is more sensitive to sources at $z \gtrsim 3$. While Planck Collaboration XXVII (2015) found that only 3.5 per cent of *Herschel*-SPIRE 350 μm-detected sources peak in the 500 μm waveband, we find that 33 per cent of the SCUBA-2-detected sources have SED models with predicted 500 μm to 350 μm flux density ratios greater than 1.

Fig. 4 shows the estimated redshift distribution of the SCUBA-2 catalogues within the *Planck* beam for the *Planck* overdensities, with 68 per cent confidence intervals. Also plotted is the expected CLS UDS redshift distribution, given the same survey area and selection function. This plot is generated by bootstrapping the Monte Carlo Markov chains (MCMC) generated by the SEDeblend method and is corrected for contributions from spurious sources by subtracting the redshift distribution of the negative SCUBA-2 sources. The majority of these negative sources have estimated redshifts greater than 6 due to the absence of associated *Herschel*-SPIRE detections and their subtraction should correct the estimated redshift distribution for contribution from spurious (positive) SCUBA-2 detections.

In order to give the CLS sources a similar selection function and flux density boosting as the overdensity fields, we add Gaussian random noise to the CLS SCUBA-2 fluxes, such that the distribution of flux density uncertainties matches the distribution of randomly selected points within the *Planck* overdensity fields with a flux density uncertainty < 4 mJy and that are within the *Planck* beam. It is important to note that this redshift distribution estimate is actually a convolution between the true redshift distribution and the redshift error distribution, and because of this, the plotted points are not independent. For the majority of sources in the $z = 1-7$ range, this error distribution function is $\delta z/(1+z) \approx 0.28$. The distribution peaks at a higher redshift than found by Planck Collaboration XXVII (2015) and due to the favourable k-correction of observing at 850 μm, this distribution may more accurately reflect the true redshift distribution of the *Planck* overdensities. If most of the *Planck* overdensities are in fact physically associated structures, then those sources found by Planck Collaboration XXVII (2015) are probably at somewhat higher redshifts and have warmer dust temperatures than assumed. Conversely, we may be detecting colder com-

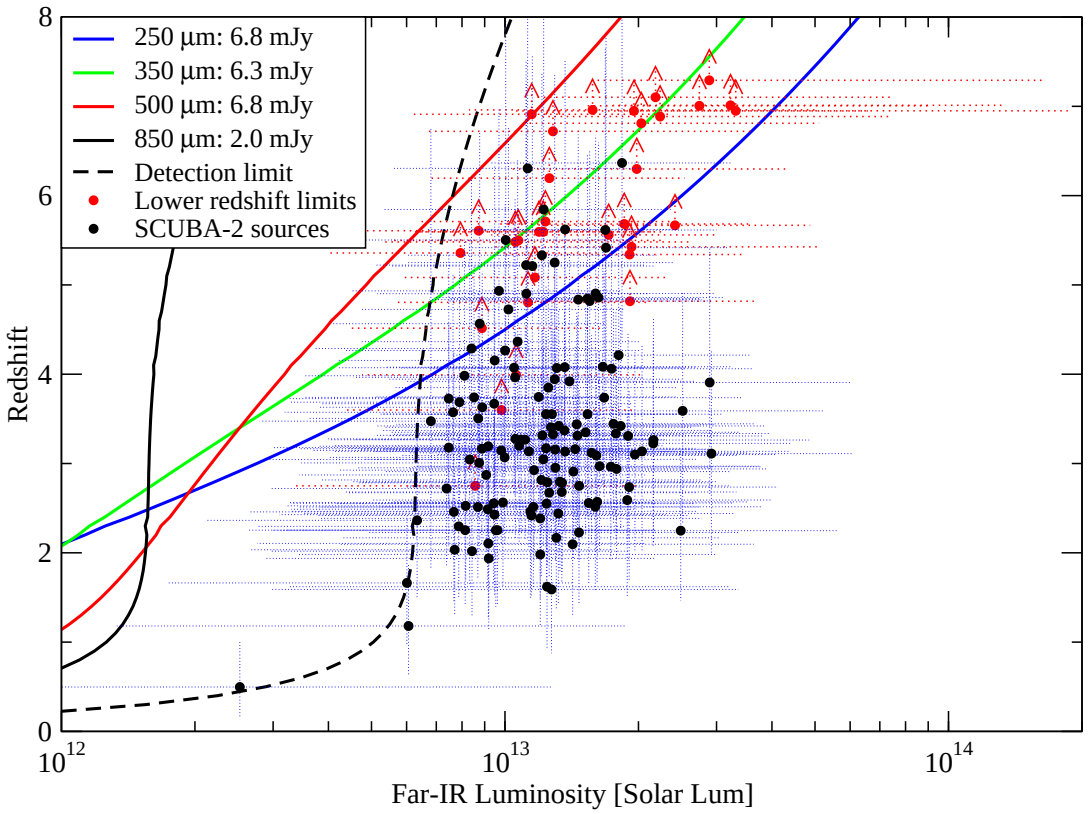


Figure 2. Constraints on far-IR luminosities and photometric redshifts for the sample of SCUBA-2-detected sources within the *Planck* "overdensity fields." We report the median values from the MCMC chains and plot 68 per cent confidence intervals for both far-IR luminosities and photometric redshifts. Photometric redshift fits for sources with redshifts greater than 6.5 are not possible due to the peak of the SED being located outside the wavelength coverage; these sources are shown with red points representing the 16 per centile of the distributions as a 1σ lower confidence limit. Solid lines denote approximate 1σ 2.0, 6.8, 6.3, and 5.8 mJy limits at 850, 500, 350, and 250 μm, respectively, for a 34 K dust temperature and $\beta = 1.5$ dust emissivity modified blackbody (the former is a representative 850 μm point source flux density uncertainty and the later are the *Herschel*-SPIRE confusion limits from Nguyen et al. 2010). Note that our source list is expected to have a rather large fraction of spurious sources (perhaps 15 per cent). When fitted, many sources get constrained to redshifts greater than 6.5, since the SPIRE images contain no nearby counterparts. For redshifts less than 6.5, we only expect nine spurious source, based on searching for negative peaks.

ponents of these structures at 850 μm. However, the redshift distribution of the SCUBA-2-selected *Planck* overdensity sources is not significantly different than those within the CLS UDS field, other than a factor of roughly 4 increase in the number of sources. Unfortunately, this finding does not help to disentangle the fraction of *Planck* sources that are line-of-sight enhancements rather than being physically associated.

Using sources within the *Planck* beams (defined to be the area above half the peak flux density within each *Planck* map) and the CLS UDS, we can assess what fraction of the *Planck* 850 μm flux density of the 51 fields we recover with SCUBA-2. To do this, we must first quantify the expected flux density contribution for a blank field (we will subtract this from the total SCUBA-2 flux density of our sources found to be within the Planck beams). Applying the same selection function of our survey to the CLS UDS source list, we recover a total flux density of 0.39 Jy per 1.05 deg^2 (the area of the Planck beams). From the Cosmic Background Explorer (*COBE*) satellite data, the total flux density of this area should be 46 Jy (although admittedly with about a 30 per cent uncertainty, Fixsen et al. 1998), thus we only recover about 1 per cent of the far-IR background in the CLS UDS field. *Planck* measured a total 850 μm flux density of 23.6 Jy within the 51 fields observed (using CMB and Galactic cirrus cleaned maps, Planck Collaboration XXXIX 2015). Summing the SCUBA-2 850 μm flux densities of the sources found to be within the Planck beams, we recover a total flux density of 1.53 Jy. Subtracting off the expected blank-field contribution estimated from the CLS UDS field, we end up with a 1.14 Jy enhancement above the background signal, and we conclude that we recover around 5 per cent of the *Planck* flux density within these fields. Comparing the relative fractions of recovered flux densities shows that the 850 μm number counts are enhanced by a larger amount at high flux densities compared to fainter sources for our survey. One must also consider that the *Planck* flux densities may have a significant flux-boosting effect, due to their low S/N and the large area used to find these overdensities; thus the fraction we recover with SCUBA-2 may be underestimated.

In Fig. 5 we estimate the co-moving SFR density for

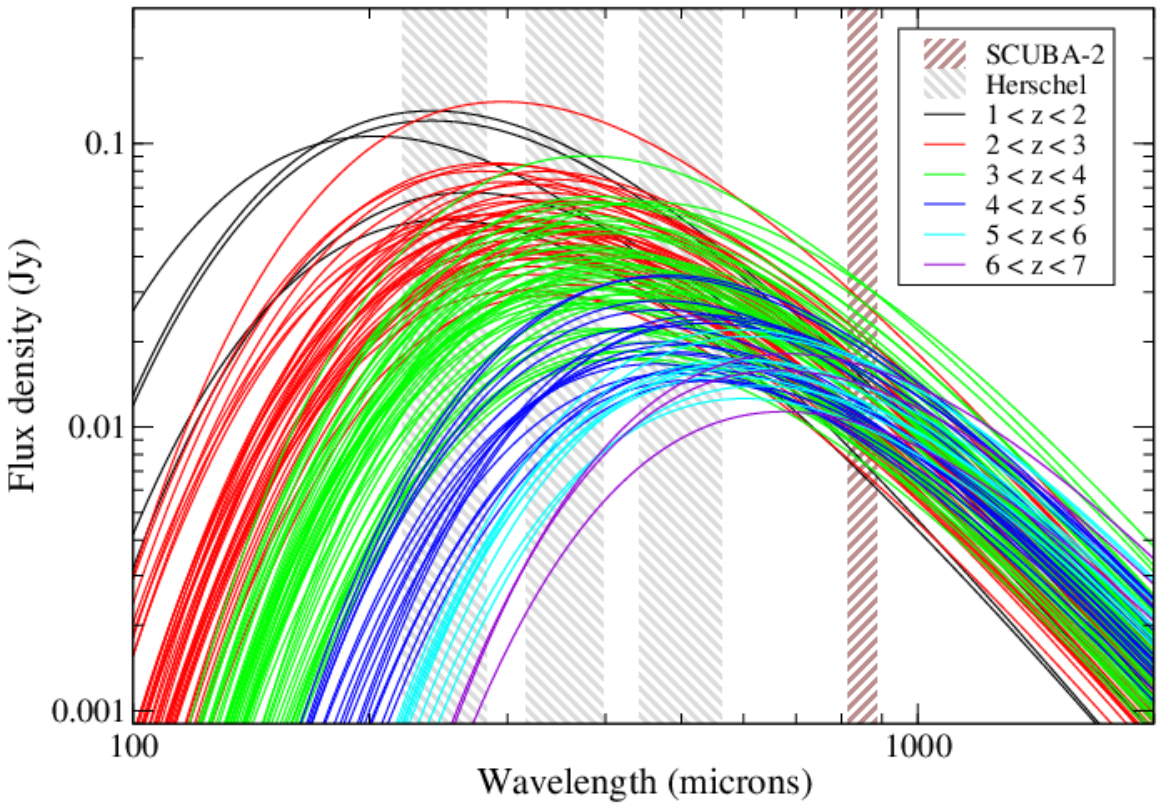


Figure 3. Model SEDs of the best-fit results for SCUBA-2 sources with constrained redshifts greater than 1. Grey and brown hatched areas denote approximate *Herschel*-SPIRE and SCUBA-2 band passes. These bandpasses are ideally located for constraining model SED parameters for sources ranging from a redshift of 1 through 7, given a source dust temperature of around 34 K.

SCUBA-2-detected *Planck* overdensity sources within the *Planck* beam and CLS UDS fields with flux densities greater than 8 mJy (and flux density uncertainty < 2 mJy) assuming a dust temperature prior of 34^{+13}_{-9} K and a conversion factor of $1.08 \times 10^{-10} \mathrm{M_{\odot} yr^{-1} L_{\odot}^{-1}}$ for a Chabrier IMF (as in, e.g. Swinbank et al. 2014). We see up to an order of magnitude increase in the SFR density in the *Planck* overdensity fields in comparison with the CLS UDS field, across a broad range of redshifts. Again, this plot is a convolution of the true comoving SFR density with the redshift error function. The plot is generated by bootstrapping the MCMC chains and is corrected for contributions from spurious sources by subtracting negative SCUBA-2 sources (although with our chosen flux cut, we only have 1 negative source to subtract from the *Planck* overdensity fields and no correction is applied to the CLS UDS field). We add noise to the CLS SCUBA-2 flux densities in order to simulate the *Planck* overdensity selection function, similar to above, but here we match the flux density uncertainty distribution of regions with uncertainty below 2 mJy. With this more strict flux density cut-off, only 0.11 deg^2 and 45 sources of the *Planck* overdensity fields remain. In comparison, an average of 70 CLS UDS sources and the majority of the original survey area are still used. This procedure gives us uncorrected number counts of 409 and 67 sources per square degree brighter than 8 mJy for the *Planck* overdensity and CLS UDS fields, respectively, i.e. the *Planck* fields contain approximately 6 times higher surface density of 850 μm sources than random parts of the sky.

6 CONCLUSIONS

We have followed up 61 *Planck* high-z candidates using SCUBA-2 on the JCMT. Of these, 10 are strong gravitational lenses, discussed in Canameras et al. (2015). The other 51 of the fields are referred to as "*Planck* overdensities" and are possible proto-cluster candidates. We have first of all confirmed, using SCUBA-2 850 μm data, that these fields do indeed represent regions of enhanced submm galaxy surface density on the sky. We have used the SEDeblend method from MacKenzie et al. (2015) and the available SCUBA-2 and *Herschel*-SPIRE observations to constrain the redshifts and far-IR luminosities of 172 SCUBA-2-detected sources. To do so, we have assumed a dust temperature prior of 34^{+13}_{-9} K and find that we achieve a redshift uncertainty of $\delta z/(1+z) \approx 0.28$ for the majority of sources.

We show that these *Planck*-selected fields have a factor of roughly 6 more sources above 8 mJy at 850 μm than blank field surveys, and that most of these sources are between a redshift of 2 and 4. These sources appear to follow approximately the same redshift distribution as those found in blank field surveys. We resolve around 5 per cent of the total *Planck* flux density. Given the same selection function, blank field surveys only recover about 1 per cent of the extragalactic far-IR background, and thus we conclude that the number counts in these fields are more enhanced at high flux densities (> 8 mJy) than at lower flux densities. We show that the SFR density in these fields are approx-

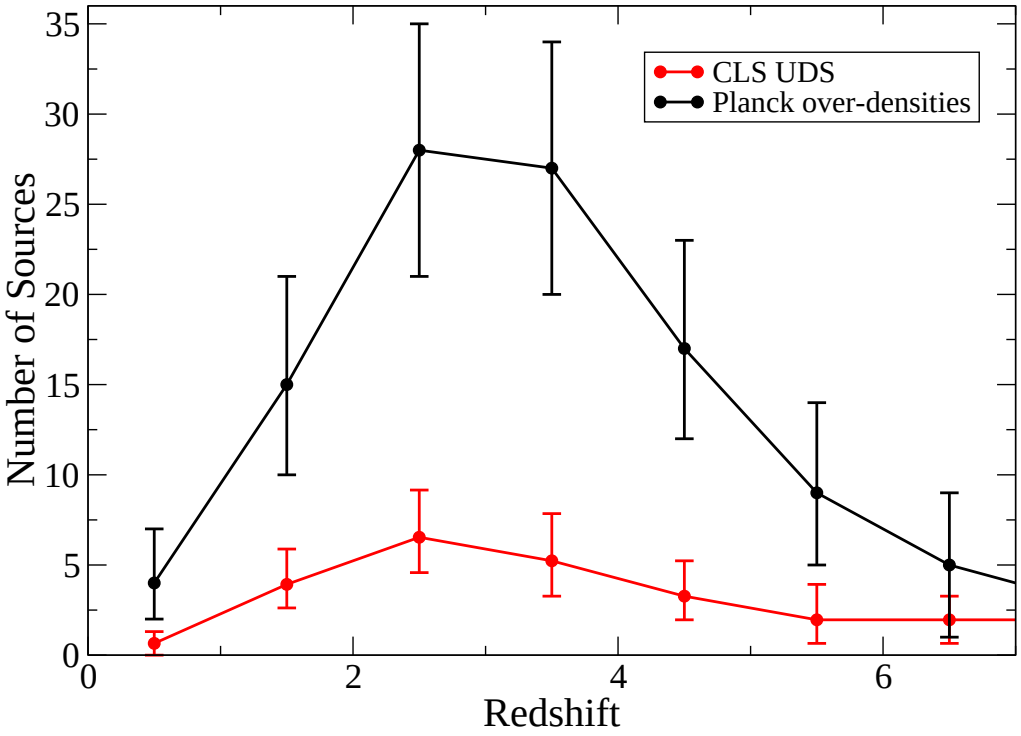


Figure 4. Redshift distribution of SCUBA-2-detected sources, assuming a dust temperature prior of 34^{+13}_{-9} K, for the *Planck* overdensity sample within the *Planck* beam. Also plotted is the expected distribution of CLS UDS sources given the same sky coverage and similar selection and flux-boosting effects. Error bars are 68 per cent confidence intervals derived from bootstrapping the sample and have been corrected for estimated contributions from spurious sources. The *Planck* overdensity fields contain a factor of about 4 more sources than the CLS UDS field, when given a similar selection function and sky coverage, but the shape of the distribution appears similar.

imately an order of magnitude higher for sources > 8 mJy for redshifts out to $z \sim 6$. Determining if the structures are in fact physically associated, or if some are simply chance alignments, will require spectroscopic redshifts at either optical or submm wavelengths. Such follow-up programmes are already underway.

ACKNOWLEDGEMENTS

This research has been supported by the Natural Sciences and Engineering Research Council of Canada. The James Clerk Maxwell Telescope is operated by the East Asian Observatory on behalf of The National Astronomical Observatory of Japan, Academia Sinica Institute of Astronomy and Astrophysics, the Korea Astronomy and Space Science Institute, the National Astronomical Observatories of China and the Chinese Academy of Sciences (Grant No. XDB09000000), with additional funding support from the Science and Technology Facilities Council of the United Kingdom and participating universities in the United Kingdom and Canada. SPIRE has been developed by a consortium of institutes led by Cardiff University (UK) and including Univ. Lethbridge (Canada); NAOC (China); CEA, LAM (France); IFSI, Univ. Padua (Italy); IAC (Spain); Stockholm Observatory (Sweden); Imperial College London, RAL, UCL-MSSL, UKATC, Univ. Sussex (UK); and Caltech, JPL, NHSC, Univ. Colorado (USA). This development has been supported by national funding agencies: CSA (Canada); NAOC (China); CEA, CNES, CNRS (France); ASI (Italy); MCINN (Spain); SNSB (Sweden); STFC, UKSA (UK); and NASA (USA). This research has made use of data from the HerMES project (`http://hermes.sussex.ac.uk/`), a Herschel Key Programme utilising Guaranteed Time from the SPIRE instrument team, ESAC scientists and a mission scientist. The HerMES data were accessed through the HeDaM database (`http://hedam.oamp.fr`) operated by CeSAM and hosted by the Laboratoire d'Astrophysique de Marseille. This research used the facilities of the Canadian Astronomy Data Centre operated by the National Research Council of Canada with the support of the Canadian Space Agency. This research was enabled in part by support provided by WestGrid (`www.westgrid.ca`) and Compute Canada Calcul Canada (`www.computecanada.ca`).

REFERENCES

Blain A. W., Longair M. S., 1993, MNRAS, 264, 509
Bleem L. E., et al., 2015, ApJS, 216, 27
Braglia F. G., et al., 2011, MNRAS, 412, 1187
Braglia F. G., Pierini D., Biviano A., Böhringer H., 2009, A&A, 500, 947
Canameras R., et al., 2015, ArXiv e-prints

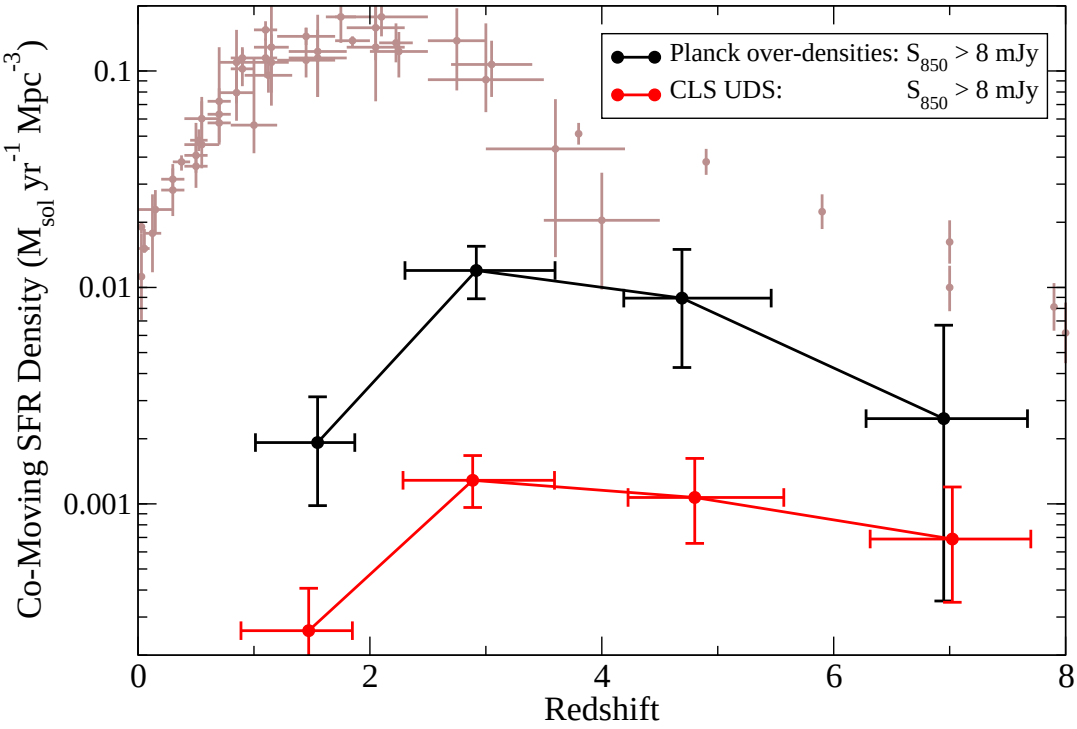


Figure 5. Co-moving SFR density versus redshift for SCUBA-2-detected sources with flux densities greater than 8 mJy assuming a dust temperature prior of 34^{+13}_{-9} K. This sample is only expected to have approximately 1 contributing spurious SCUBA-2 source. For comparison, we also show results from fitting to sources within the CLS UDS field, using the same technique, with a similar selection and flux-boosting effects. An order of magnitude increase in star-formation rate density is seen across all redshifts. The light brown points are measurements of the global co-moving star-formation density from an assortment of sources, as compiled by Madau & Dickinson (2014).

Chapin E. L., Berry D. S., Gibb A. G., Jenness T., Scott D., Tilanus R. P. J., Economou F., Holland W. S., 2013, MNRAS, 430, 2545

Chapman S. C., Blain A. W., Smail I., Ivison R. J., 2005, ApJ, 622, 772

Clements D. L., et al., 2014, MNRAS, 439, 1193

Clements D. L., Sutherland W. J., McMahon R. G., Saunders W., 1996, MNRAS, 279, 477

Combes F., et al., 2012, A&A, 538, L4

Coppin K., et al., 2006, MNRAS, 372, 1621

Daddi E., Dickinson M., Morrison G., Chary R., Cimatti A., Elbaz D., Frayer D., Renzini A., Pope A., Alexander D. M., Bauer F. E., Giavalisco M., Huynh M., Kurk J., Mignoli M., 2007, ApJ, 670, 156

Dempsey J., Friberg P., 2008, SPIE, 7012, 137

Dempsey J. T., et al., 2013, MNRAS, 430, 2534

Dempsey J. T., Friberg P., Jenness T., Bintley D., Holland W. S., 2010 Vol. 7741 of Society of Photo-Optical Instrumentation Engineers (SPIE) Conference Series, Extinction correction and on-sky calibration of SCUBA-2. p. 1

Eisenhardt P. R. M., Brodwin M., Gonzalez A. H., Stanford S. A., Stern D., Barmby P., Brown M. J. I., Dawson K., Dey A., Doi M., Galametz A., Jannuzi B. T., Kochanek C. S., Meyers J., Morokuma T., Moustakas L. A., 2008, ApJ, 684, 905

Elbaz D., et al., 2011, A&A, 533, A119

Fixsen D. J., Dwek E., Mather J. C., Bennett C. L., Shafer R. A., 1998, ApJ, 508, 123

Franceschini A., Toffolatti L., Mazzei P., Danese L., de Zotti G., 1991, A&AS, 89, 285

Fu H., et al., 2012, ApJ, 753, 134

Gibb A., Jenness T., 2010, Processing SCUBA-2 Data with ORAC-DR, Starlink User Note 264, Version 1.0.0, `http://www.starlink.ac.uk/docs/sun264.htx/sun264.html`

Griffin M. J., et al., 2010, å, 518, L3

Hasselfield M., et al., 2013, J. Cosmology Astropart. Phys., 7, 8

Hastings W. K., 1970, Biometrika, 57, 97

Holland W. S., Robson E. I., Gear W. K., Cunningham C. R., Lightfoot J. F., Jenness T., Ivison R. J., Stevens J. A., Ade P. A. R., Griffin M. J., Duncan W. D., Murphy J. A., Naylor D. A., 1999, MNRAS, 303, 659

Lawrence A., et al., 2007, MNRAS, 379, 1599

MacKenzie T., Scott D., Swinbank M., 2015, ArXiv e-prints

MacKenzie T. P., et al., 2014, MNRAS, 445, 201

Madau P., Dickinson M., 2014, ARA&A, 52, 415

Metropolis N., Rosenbluth A. W., Rosenbluth M. N., Teller A. H., Teller E., 1953, JCP, 21, 1087

Murphy Jr. T. W., Armus L., Matthews K., Soifer B. T., Mazzarella J. M., Shupe D. L., Strauss M. A., Neugebauer G., 1996, AJ, 111, 1025

Negrello M., et al., 2010, Science, 330, 800

Nguyen H. T., et al., 2010, A&A, 518, L5

Noeske K. G., et al., 2007, ApJ, 660, L43

Oliver S. J., et al., 2012, MNRAS, 424, 1614

Ott S., 2010, in Mizumoto Y., Morita K.-I., Ohishi M., eds, Astronomical Data Analysis Software and Systems XIX Vol. 434 of Astronomical Society of the Pacific Conference Series, The Herschel Data Processing System – HIPE and Pipelines – Up and Running Since the Start of the Mission. p. 139
Pascale E., et al., 2008, ApJ, 681, 400
Pilbratt G. L., Riedinger J. R., Passvogel T., Crone G., Doyle D., Gageur U., Heras A. M., Jewell C., Metcalfe L., Ott S., Schmidt M., 2010, A&A, 518, L1
Planck Collaboration VII 2011, A&A, 536, A7
Planck Collaboration VIII 2011, A&A, 536, A8
Planck Collaboration XIII 2015, ArXiv e-prints
Planck Collaboration XX 2014, A&A, 571, A20
Planck Collaboration XXIX 2014, A&A, 571, A29
Planck Collaboration XXVII 2015, ArXiv e-prints
Planck Collaboration XXVIII 2014, AAP, 571, A28
Planck Collaboration XXXIX 2015, ArXiv e-prints
Sanders D. B., Mirabel I. F., 1996, ARA&A, 34, 749
Scott K. S., et al., 2010, MNRAS, 405, 2260
Simpson J., et al., 2015, ArXiv e-prints
Simpson J. M., et al., 2014, ApJ, 788, 125
Swinbank A. M., et al., 2014, MNRAS, 438, 1267
Verdugo M., Ziegler B. L., Gerken B., 2008, A&A, 486, 9

Table 1: SCUBA-2-detected sources within the *Planck* proto-cluster candidate fields. Flux density uncertainties at 850 μm are instrumental noise only and do not include confusion noise. We report the median values from the MCMC chains and 68 per cent confidence intervals for both far-IR luminosities and photometric redshifts. Photometric redshift fits for sources with redshifts greater than about 6.5 are not possible, due to the peak of the SED being located outside the wavelength coverage. For these sources, we provide the 16th per centile of the distributions as a 1σ lower confidence limit.

Galaxy ID	RA J2000	Dec J2000	S_{850} (mJy)	$z_{\rm phot}$	Far-IR luminosity ($L_\odot$)	In *Planck* beam
PCCS_G045.7-41.2-0	21:39:51.055	−8:47:16.80	13.1 ± 2.5	$4.1^{+1.6}_{-1.3}$	$1.7^{+1.9}_{-1.1} \times 10^{13}$	Y
PCCS_G045.7-41.2-1	21:39:30.820	−8:44:08.79	11.1 ± 2.4	$2.7^{+1.0}_{-0.9}$	$1.3^{+1.5}_{-0.8} \times 10^{13}$	Y
PCCS_G045.7-41.2-2	21:39:47.817	−8:44:20.80	9.9 ± 2.1	$0.1^{+0.1}_{-0.1}$	$9.7^{+46.4}_{-8.4} \times 10^{10}$	Y
PCCS_G045.7-41.2-3	21:39:29.200	−8:46:04.78	13.1 ± 3.2	$3.9^{+1.4}_{-1.2}$	$1.4^{+1.3}_{-0.8} \times 10^{13}$	N
PCCS_G059.1-67.1-0	23:26:25.977	−15:28:05.40	14.5 ± 1.6	$3.3^{+1.3}_{-1.1}$	$1.5^{+1.6}_{-0.9} \times 10^{13}$	Y
PCCS_G059.1-67.1-1	23:26:01.346	−15:30:45.32	18.1 ± 3.8	> 7.0	$2.7^{+6.3}_{-1.2} \times 10^{13}$	N
PCCS_G059.1-67.1-2	23:26:41.749	−15:28:57.36	13.3 ± 2.8	$3.3^{+1.2}_{-1.0}$	$1.2^{+1.2}_{-0.7} \times 10^{13}$	N
PCCS_G059.1-67.1-3	23:26:47.004	−15:27:17.34	14.8 ± 3.5	> 7.1	$2.2^{+5.2}_{-1.0} \times 10^{13}$	N
PCCS_G073.4-57.5-0	23:14:42.344	−4:16:40.20	10.4 ± 1.8	$2.6^{+1.0}_{-0.9}$	$9.4^{+11.0}_{-6.1} \times 10^{12}$	Y
PCCS_G073.4-57.5-1	23:14:42.611	−4:20:00.20	13.6 ± 2.5	$4.8^{+1.7}_{-1.4}$	$1.6^{+1.4}_{-0.8} \times 10^{13}$	N
PCCS_G073.4-57.5-2	23:14:41.809	−4:17:44.20	8.3 ± 2.0	> 3.6	$9.8^{+9.9}_{-5.5} \times 10^{12}$	Y
PCCS_G073.4-57.5-3	23:14:34.589	−4:17:00.20	7.2 ± 1.8	$3.7^{+1.5}_{-1.2}$	$7.9^{+8.2}_{-4.6} \times 10^{12}$	Y
PHZ_G038.0-51.5-0	22:08:50.400	−17:55:47.90	15.9 ± 2.0	$2.7^{+1.1}_{-1.0}$	$1.9^{+2.2}_{-1.3} \times 10^{13}$	Y
PHZ_G038.0-51.5-1	22:08:48.438	−17:57:35.90	10.3 ± 2.0	$3.1^{+1.2}_{-1.1}$	$1.1^{+1.3}_{-0.7} \times 10^{13}$	Y
PHZ_G038.0-51.5-2	22:08:45.353	−17:59:27.90	10.4 ± 2.4	$2.3^{+0.9}_{-0.9}$	$9.5^{+12.3}_{-6.5} \times 10^{12}$	Y
PHZ_G067.2-63.8-0	23:24:24.799	−10:43:46.08	22.7 ± 3.5	$3.1^{+1.2}_{-1.1}$	$2.0^{+2.3}_{-1.3} \times 10^{13}$	N
PHZ_G067.2-63.8-10	23:24:27.248	−10:51:10.07	11.8 ± 2.8	$4.1^{+1.6}_{-1.3}$	$1.3^{+1.2}_{-0.7} \times 10^{13}$	N
PHZ_G067.2-63.8-11	23:24:12.314	−10:48:06.10	5.9 ± 1.5	> 5.4	$7.9^{+8.2}_{-3.9} \times 10^{12}$	Y
PHZ_G067.2-63.8-1	23:24:12.043	−10:46:14.10	11.1 ± 1.8	$2.6^{+1.0}_{-0.9}$	$1.2^{+1.4}_{-0.8} \times 10^{13}$	Y
PHZ_G067.2-63.8-2	23:24:23.718	−10:50:18.08	12.6 ± 2.1	$3.0^{+1.3}_{-1.0}$	$1.6^{+2.1}_{-1.0} \times 10^{13}$	N
PHZ_G067.2-63.8-3	23:24:01.728	−10:45:26.09	13.1 ± 2.2	$4.9^{+1.8}_{-1.5}$	$1.6^{+1.4}_{-0.9} \times 10^{13}$	Y
PHZ_G067.2-63.8-4	23:24:00.643	−10:45:06.09	11.9 ± 2.2	$2.7^{+1.3}_{-1.0}$	$1.3^{+2.0}_{-0.9} \times 10^{13}$	Y
PHZ_G067.2-63.8-5	23:24:16.658	−10:48:30.10	7.8 ± 1.7	$3.6^{+1.5}_{-1.1}$	$8.9^{+9.4}_{-5.1} \times 10^{12}$	Y
PHZ_G067.2-63.8-6	23:24:06.614	−10:47:14.10	7.1 ± 1.5	$2.3^{+0.9}_{-0.8}$	$8.1^{+9.9}_{-5.5} \times 10^{12}$	Y
PHZ_G067.2-63.8-7	23:23:56.023	−10:51:30.08	10.7 ± 2.4	$1.6^{+0.8}_{-0.7}$	$1.3^{+2.1}_{-1.0} \times 10^{13}$	N
PHZ_G067.2-63.8-8	23:24:01.453	−10:52:06.09	8.9 ± 2.1	$6.3^{+2.3}_{-2.1}$	$1.1^{+0.9}_{-0.6} \times 10^{13}$	Y
PHZ_G067.2-63.8-9	23:23:59.014	−10:45:34.08	8.6 ± 2.1	$3.5^{+1.4}_{-1.1}$	$8.7^{+8.7}_{-5.1} \times 10^{12}$	Y
PHZ_G103.1-73.6-0	0:28:48.011	−11:35:52.39	9.0 ± 2.2	> 4.0	$1.1^{+1.0}_{-0.6} \times 10^{13}$	Y
PHZ_G106.8-83.3-0	0:43:25.677	−20:36:20.29	22.8 ± 1.7	$3.6^{+1.3}_{-1.3}$	$2.5^{+2.7}_{-1.6} \times 10^{13}$	Y
PHZ_G106.8-83.3-10	0:43:12.001	−20:37:36.29	7.0 ± 1.6	$3.6^{+1.5}_{-1.2}$	$7.6^{+8.3}_{-4.4} \times 10^{12}$	Y
PHZ_G106.8-83.3-1	0:43:17.415	−20:36:00.30	10.2 ± 1.4	$2.2^{+0.9}_{-0.8}$	$1.5^{+1.9}_{-1.0} \times 10^{13}$	Y
PHZ_G106.8-83.3-11	0:43:29.099	−20:38:44.28	8.1 ± 2.0	$4.9^{+2.0}_{-1.6}$	$9.7^{+8.5}_{-5.2} \times 10^{12}$	Y
PHZ_G106.8-83.3-12	0:43:17.700	−20:36:48.30	5.9 ± 1.4	$2.3^{+1.0}_{-0.8}$	$7.9^{+10.9}_{-5.1} \times 10^{12}$	Y
PHZ_G106.8-83.3-2	0:43:14.281	−20:36:12.30	10.1 ± 1.4	$2.4^{+1.1}_{-0.9}$	$9.5^{+13.6}_{-6.4} \times 10^{12}$	Y
PHZ_G106.8-83.3-3	0:43:21.689	−20:36:40.30	9.1 ± 1.5	$5.2^{+2.3}_{-1.7}$	$1.1^{+0.9}_{-0.6} \times 10^{13}$	Y
PHZ_G106.8-83.3-4	0:43:02.320	−20:34:04.26	12.4 ± 2.1	$2.6^{+1.0}_{-0.9}$	$1.5^{+1.7}_{-1.0} \times 10^{13}$	Y
PHZ_G106.8-83.3-5	0:43:32.230	−20:36:48.26	12.0 ± 2.1	$2.7^{+1.1}_{-0.8}$	$1.5^{+1.7}_{-0.9} \times 10^{13}$	Y
PHZ_G106.8-83.3-6	0:43:41.064	−20:37:20.20	19.1 ± 3.9	> 7.0	$3.2^{+9.9}_{-1.5} \times 10^{13}$	N
PHZ_G106.8-83.3-7	0:43:04.598	−20:34:24.27	9.4 ± 2.0	$3.3^{+1.2}_{-1.1}$	$1.1^{+1.1}_{-0.7} \times 10^{13}$	Y
PHZ_G106.8-83.3-8	0:43:04.882	−20:34:52.27	8.7 ± 1.9	$4.7^{+2.1}_{-1.6}$	$1.0^{+0.8}_{-0.5} \times 10^{13}$	Y
PHZ_G106.8-83.3-9	0:43:32.807	−20:40:44.26	13.9 ± 3.1	$3.9^{+1.6}_{-1.2}$	$1.3^{+1.2}_{-0.7} \times 10^{13}$	Y
PHZ_G119.4-76.6-0	0:48:10.840	−13:45:56.30	24.5 ± 2.2	$3.1^{+1.1}_{-1.1}$	$2.9^{+3.1}_{-1.9} \times 10^{13}$	Y
PHZ_G119.4-76.6-1	0:47:52.723	−13:41:56.28	10.7 ± 1.9	$2.6^{+1.0}_{-1.1}$	$1.9^{+2.1}_{-1.4} \times 10^{13}$	Y
PHZ_G119.4-76.6-2	0:48:10.016	−13:44:28.30	10.8 ± 2.4	$3.7^{+1.5}_{-1.2}$	$1.2^{+1.3}_{-0.7} \times 10^{13}$	Y
PHZ_G119.4-76.6-3	0:47:59.311	−13:40:32.30	7.4 ± 1.7	> 5.5	$1.1^{+1.6}_{-0.5} \times 10^{13}$	Y
PHZ_G119.4-76.6-4	0:48:02.604	−13:40:12.30	7.0 ± 1.7	> 2.7	$8.6^{+11.3}_{-5.2} \times 10^{12}$	Y
PHZ_G119.4-76.6-5	0:47:53.273	−13:41:12.28	7.6 ± 1.8	> 5.5	$1.1^{+1.2}_{-0.5} \times 10^{13}$	Y
PHZ_G119.4-76.6-6	0:48:08.093	−13:37:24.30	9.2 ± 2.2	> 5.6	$1.2^{+1.1}_{-0.6} \times 10^{13}$	N
PHZ_G119.4-76.6-7	0:47:45.864	−13:39:36.26	10.0 ± 2.5	$2.3^{+0.9}_{-0.8}$	$9.6^{+12.1}_{-6.4} \times 10^{12}$	N
PHZ_G119.4-76.6-8	0:48:13.584	−13:43:12.29	8.1 ± 2.0	> 6.9	$1.1^{+1.2}_{-0.5} \times 10^{13}$	Y
PHZ_G132.6-81.1-0	0:57:48.895	−18:19:23.50	13.3 ± 2.1	$3.3^{+1.4}_{-1.2}$	$1.5^{+1.8}_{-1.0} \times 10^{13}$	Y
PHZ_G132.6-81.1-1	0:57:52.265	−18:19:03.49	8.6 ± 2.1	> 4.8	$1.1^{+1.0}_{-0.6} \times 10^{13}$	Y
PHZ_G171.1-78.7-0	1:27:01.926	−19:19:41.60	14.6 ± 2.1	$3.1^{+1.1}_{-1.1}$	$1.6^{+1.7}_{-1.0} \times 10^{13}$	Y
PHZ_G171.1-78.7-1	1:26:50.339	−19:20:13.56	15.4 ± 3.6	$5.4^{+2.4}_{-1.7}$	$1.7^{+1.5}_{-0.9} \times 10^{13}$	Y
PHZ_G171.1-78.7-2	1:27:08.708	−19:18:57.60	9.0 ± 2.1	$4.9^{+2.4}_{-1.7}$	$1.1^{+1.0}_{-0.6} \times 10^{13}$	Y
PHZ_G171.1-78.7-3	1:27:08.708	−19:19:01.60	8.7 ± 2.1	$4.0^{+2.0}_{-1.3}$	$1.1^{+1.0}_{-0.6} \times 10^{13}$	Y
PHZ_G173.9+57.0-0	10:28:38.124	43:25:37.69	8.5 ± 1.9	$3.7^{+1.6}_{-1.2}$	$9.5^{+9.9}_{-5.6} \times 10^{12}$	Y
PHZ_G173.9+57.0-1	10:28:48.771	43:24:53.70	8.7 ± 2.0	$2.4^{+1.0}_{-0.9}$	$1.1^{+1.5}_{-0.8} \times 10^{13}$	Y
PHZ_G176.6+59.0-0	10:36:56.556	41:27:22.40	15.8 ± 2.6	$3.3^{+1.2}_{-1.2}$	$1.9^{+1.9}_{-1.2} \times 10^{13}$	Y
PHZ_G176.6+59.0-1	10:37:05.451	41:27:30.38	12.5 ± 3.0	$2.1^{+1.0}_{-0.8}$	$1.4^{+2.2}_{-1.0} \times 10^{13}$	Y
PHZ_G214.1+48.3-0	9:52:34.268	19:08:18.69	15.7 ± 3.1	$6.4^{+2.2}_{-2.0}$	$1.8^{+1.4}_{-0.9} \times 10^{13}$	Y
PHZ_G214.1+48.3-1	9:52:39.349	19:08:30.67	14.9 ± 3.2	> 6.9	$2.2^{+5.1}_{-1.0} \times 10^{13}$	Y
PHZ_G214.1+48.3-2	9:52:09.714	19:06:26.66	15.2 ± 3.6	$5.6^{+2.1}_{-1.6}$	$1.7^{+1.3}_{-0.8} \times 10^{13}$	N

Gal ID	RA J2000	Dec J2000	S_{850} (mJy)	$z_{\rm phot}$	Far-IR Luminosity ($L_\odot$)	In Planck Beam
Planck18p194-0	8:30:46.455	19:36:47.19	19.6 ± 1.9	$3.3^{+1.4}_{-1.1}$	$2.2^{+2.7}_{-1.4} \times 10^{13}$	Y
Planck18p194-1	8:30:54.382	19:37:31.20	14.9 ± 1.7	$3.3^{+1.4}_{-1.2}$	$1.8^{+2.2}_{-1.1} \times 10^{13}$	Y
Planck18p194-2	8:30:51.551	19:37:55.20	10.7 ± 1.6	$5.3^{+2.1}_{-1.7}$	$1.3^{+1.1}_{-0.7} \times 10^{13}$	Y
Planck18p194-3	8:30:41.073	19:39:43.18	13.7 ± 2.5	$4.9^{+1.7}_{-1.5}$	$1.6^{+1.5}_{-0.9} \times 10^{13}$	Y
Planck18p194-4	8:31:04.287	19:34:23.18	13.7 ± 3.1	$3.4^{+1.3}_{-1.1}$	$1.5^{+1.5}_{-0.9} \times 10^{13}$	N
Planck18p194-5	8:30:40.228	19:36:15.17	8.5 ± 2.0	> 6.7	$1.3^{+2.3}_{-0.6} \times 10^{13}$	Y
Planck18p194-6	8:30:51.268	19:37:31.20	6.8 ± 1.7	$3.2^{+1.2}_{-1.0}$	$8.9^{+9.7}_{-5.4} \times 10^{12}$	Y
Planck18p194-7	8:30:48.719	19:37:55.20	6.5 ± 1.6	$4.0^{+1.5}_{-1.2}$	$8.1^{+7.8}_{-4.6} \times 10^{12}$	Y
Planck18p735-0	1:58:48.085	−7:52:43.50	8.5 ± 2.0	$2.8^{+1.2}_{-1.0}$	$1.3^{+1.7}_{-0.9} \times 10^{13}$	Y
Planck24p194-0	8:40:40.588	22:12:37.60	8.3 ± 1.6	$2.8^{+1.1}_{-0.9}$	$1.2^{+1.4}_{-0.8} \times 10^{13}$	Y
PLCK_G006.1+61.8-0	14:33:47.1	12:12:60.00	16.0 ± 2.8	$2.8^{+1.1}_{-1.0}$	$1.3^{+1.6}_{-0.9} \times 10^{13}$	Y
PLCK_G006.1+61.8-1	14:33:39.817	12:14:52.00	14.0 ± 3.0	$3.7^{+1.4}_{-1.1}$	$1.7^{+1.8}_{-1.0} \times 10^{13}$	Y
PLCK_G009.8+72.6-0	13:59:19.151	19:19:15.97	18.7 ± 2.2	$3.2^{+1.2}_{-1.1}$	$2.2^{+2.3}_{-1.4} \times 10^{13}$	Y
PLCK_G009.8+72.6-1	13:59:02.479	19:19:32.00	10.1 ± 2.2	$5.3^{+2.0}_{-1.6}$	$1.2^{+1.0}_{-0.6} \times 10^{13}$	Y
PLCK_G009.8+72.6-2	13:59:28.188	19:16:27.92	11.9 ± 2.9	$3.9^{+1.4}_{-1.2}$	$1.3^{+1.2}_{-0.7} \times 10^{13}$	N
PLCK_G009.8+72.6-3	13:58:57.958	19:18:15.99	11.1 ± 2.7	$5.8^{+3.0}_{-2.8}$	$1.2^{+1.1}_{-0.7} \times 10^{13}$	Y
PLCK_G049.6-42.9-0	21:51:38.531	−7:05:06.90	9.9 ± 1.6	$2.4^{+1.0}_{-0.9}$	$1.2^{+1.6}_{-0.8} \times 10^{13}$	Y
PLCK_G049.6-42.9-1	21:51:41.219	−7:05:54.90	7.8 ± 1.9	$2.7^{+1.1}_{-0.9}$	$7.4^{+8.4}_{-4.4} \times 10^{12}$	Y
PLCK_G049.6-42.9-2	21:51:33.694	−7:05:02.90	6.5 ± 1.6	> 5.6	$8.7^{+8.5}_{-4.3} \times 10^{12}$	Y
PLCK_G056.7+62.6-0	14:54:39.298	34:43:28.00	15.9 ± 2.7	$2.9^{+1.2}_{-1.0}$	$1.8^{+2.1}_{-1.2} \times 10^{13}$	Y
PLCK_G056.7+62.6-1	14:54:38.649	34:46:24.00	10.7 ± 2.4	$3.2^{+1.3}_{-1.1}$	$1.3^{+1.6}_{-0.8} \times 10^{13}$	Y
PLCK_G056.7+62.6-2	14:54:28.259	34:47:11.98	14.4 ± 3.3	$3.6^{+1.4}_{-1.1}$	$1.2^{+1.2}_{-0.7} \times 10^{13}$	Y
PLCK_G068.3+31.9-0	17:33:13.960	42:42:21.70	18.8 ± 2.8	$2.2^{+0.9}_{-0.8}$	$2.5^{+3.1}_{-1.6} \times 10^{13}$	Y
PLCK_G068.3+31.9-1	17:33:32.479	42:45:09.63	14.4 ± 3.6	$3.3^{+1.2}_{-1.0}$	$1.3^{+1.3}_{-0.7} \times 10^{13}$	N
PLCK_G075.1+33.2-0	17:29:51.000	48:31:35.00	13.1 ± 2.7	$6.2^{+1.6}_{-2.2}$	$1.5^{+1.0}_{-0.8} \times 10^{13}$	Y
PLCK_G077.7+32.6-0	17:33:47.863	50:44:56.17	14.9 ± 3.7	$2.0^{+0.8}_{-0.7}$	$8.4^{+10.5}_{-5.5} \times 10^{12}$	N
PLCK_G078.9+48.2-0	15:56:11.488	50:04:32.77	12.8 ± 2.4	$4.1^{+1.5}_{-1.4}$	$1.4^{+1.3}_{-0.8} \times 10^{13}$	Y
PLCK_G078.9+48.2-1	15:55:36.170	50:04:28.63	14.2 ± 3.3	> 5.4	$1.9^{+3.2}_{-1.0} \times 10^{13}$	Y
PLCK_G082.5+38.4-0	16:55:59.511	54:30:00.89	18.1 ± 2.0	> 7.0	$3.3^{+15.3}_{-1.5} \times 10^{13}$	Y
PLCK_G082.5+38.4-1	16:55:31.952	54:30:36.77	11.6 ± 2.8	$2.0^{+0.9}_{-0.7}$	$7.7^{+9.8}_{-5.0} \times 10^{12}$	Y
PLCK_G082.5+38.4-2	16:55:39.750	54:32:28.85	10.1 ± 2.5	$2.5^{+0.9}_{-0.8}$	$8.2^{+8.9}_{-5.0} \times 10^{12}$	N
PLCK_G083.3+51.0-0	15:33:13.312	51:47:39.00	12.2 ± 2.2	$3.4^{+1.3}_{-1.1}$	$1.3^{+1.4}_{-0.8} \times 10^{13}$	Y
PLCK_G083.3+51.0-1	15:32:51.293	51:52:06.92	16.5 ± 3.5	$4.1^{+1.5}_{-1.3}$	$1.7^{+1.6}_{-1.0} \times 10^{13}$	Y
PLCK_G083.3+51.0-2	15:32:57.793	51:46:54.97	13.0 ± 2.9	$3.2^{+1.7}_{-1.0}$	$9.2^{+10.0}_{-5.4} \times 10^{12}$	Y
PLCK_G084.0-71.5-0	0:04:16.645	−12:18:09.58	16.5 ± 2.6	$4.2^{+1.5}_{-1.3}$	$1.8^{+1.8}_{-1.0} \times 10^{13}$	Y
PLCK_G084.0-71.5-1	0:04:17.194	−12:14:05.58	15.5 ± 3.6	> 4.8	$1.9^{+1.7}_{-1.0} \times 10^{13}$	N
PLCK_G084.0-71.5-2	0:04:30.019	−12:17:53.60	9.1 ± 2.2	> 5.6	$1.2^{+1.0}_{-0.6} \times 10^{13}$	Y
PLCK_G091.9+43.0-0	16:09:59.845	60:19:52.00	17.2 ± 3.2	$3.6^{+1.3}_{-1.2}$	$1.5^{+1.6}_{-0.9} \times 10^{13}$	Y
PLCK_G091.9+43.0-1	16:10:14.926	60:19:15.96	15.5 ± 3.1	$3.4^{+1.3}_{-1.1}$	$1.8^{+1.9}_{-1.1} \times 10^{13}$	Y
PLCK_G093.6+55.9-0	14:44:05.173	54:16:45.00	17.3 ± 3.7	> 5.7	$2.4^{+2.5}_{-1.2} \times 10^{13}$	N
PLCK_G093.6+55.9-1	14:43:56.475	54:21:16.97	11.5 ± 2.5	$3.1^{+1.3}_{-1.0}$	$1.6^{+1.9}_{-1.0} \times 10^{13}$	Y
PLCK_G132.9-76.0-0	1:01:00.549	−13:17:54.25	16.1 ± 3.8	$2.6^{+1.0}_{-0.9}$	$1.6^{+1.9}_{-1.1} \times 10^{13}$	N
PLCK_G144.1+81.0-0	12:35:34.282	35:28:40.50	13.0 ± 2.7	$3.4^{+1.3}_{-1.0}$	$1.3^{+1.4}_{-0.7} \times 10^{13}$	Y
PLCK_G144.1+81.0-1	12:35:46.730	35:30:08.45	14.2 ± 3.5	> 6.3	$2.0^{+2.4}_{-1.0} \times 10^{13}$	N
PLCK_G160.7+41.0-0	9:07:54.534	56:03:10.89	22.3 ± 3.9	$3.9^{+1.5}_{-1.3}$	$2.9^{+3.2}_{-1.7} \times 10^{13}$	Y
PLCK_G162.1-59.3-0	2:06:51.367	−2:16:05.80	8.1 ± 1.6	$2.5^{+1.0}_{-0.9}$	$9.1^{+10.7}_{-5.9} \times 10^{12}$	Y
PLCK_G162.1-59.3-1	2:06:39.892	−2:11:21.80	14.3 ± 3.2	$3.1^{+1.1}_{-1.1}$	$2.0^{+2.1}_{-1.3} \times 10^{13}$	Y
PLCK_G162.1-59.3-2	2:06:39.090	−2:16:57.80	8.4 ± 2.0	$3.1^{+1.2}_{-1.1}$	$9.8^{+10.9}_{-6.1} \times 10^{12}$	N
PLCK_G162.1-59.3-3	2:06:49.232	−2:15:49.80	6.8 ± 1.6	> 4.5	$8.9^{+7.9}_{-4.5} \times 10^{12}$	Y
PLCK_G165.8+45.3-0	9:30:34.209	51:28:06.19	14.2 ± 3.5	> 5.7	$1.9^{+1.7}_{-0.9} \times 10^{13}$	N
PLCK_G173.8+59.3-0	10:40:31.859	42:43:23.00	12.6 ± 2.1	$3.2^{+1.3}_{-1.1}$	$1.2^{+1.4}_{-0.8} \times 10^{13}$	Y
PLCK_G173.8+59.3-1	10:40:30.765	42:48:11.00	17.1 ± 3.4	> 7.3	$2.9^{+13.7}_{-1.3} \times 10^{13}$	Y
PLCK_G177.0+35.9-0	8:30:58.465	43:40:11.16	11.0 ± 2.3	$5.6^{+1.9}_{-1.6}$	$1.4^{+1.1}_{-0.7} \times 10^{13}$	N
PLCK_G177.0+35.9-1	8:31:13.948	43:38:03.20	8.1 ± 1.7	$1.7^{+0.7}_{-0.7}$	$6.0^{+8.2}_{-4.3} \times 10^{12}$	Y
PLCK_G177.0+35.9-2	8:31:18.741	43:39:39.18	8.6 ± 1.8	$5.5^{+2.8}_{-2.0}$	$1.0^{+0.9}_{-0.5} \times 10^{13}$	Y
PLCK_G177.0+35.9-3	8:31:41.579	43:37:50.95	14.9 ± 3.4	> 5.3	$1.9^{+1.6}_{-0.9} \times 10^{13}$	N
PLCK_G177.0+35.9-4	8:31:02.153	43:39:59.18	9.0 ± 2.2	$0.5^{+0.5}_{-0.3}$	$2.5^{+10.3}_{-2.3} \times 10^{12}$	Y
PLCK_G179.3+50.7-0	9:51:38.990	41:39:15.59	12.2 ± 1.6	$2.8^{+1.2}_{-1.1}$	$1.2^{+1.6}_{-0.8} \times 10^{13}$	Y
PLCK_G179.3+50.7-1	9:51:41.131	41:39:43.60	8.4 ± 1.5	$2.9^{+1.2}_{-1.0}$	$9.1^{+11.6}_{-5.6} \times 10^{12}$	Y
PLCK_G179.3+50.7-2	9:51:44.700	41:40:07.60	7.0 ± 1.5	$3.7^{+1.7}_{-1.2}$	$7.5^{+7.5}_{-4.2} \times 10^{12}$	Y
PLCK_G179.3+50.7-3	9:52:00.771	41:41:47.53	9.0 ± 2.0	$4.3^{+1.6}_{-1.4}$	$1.0^{+1.0}_{-0.6} \times 10^{13}$	Y
PLCK_G179.3+50.7-4	9:51:45.413	41:35:39.60	10.6 ± 2.4	> 7.0	$1.6^{+3.5}_{-0.7} \times 10^{13}$	N
PLCK_G179.3+50.7-5	9:51:45.414	41:37:59.60	7.3 ± 1.7	$3.2^{+1.4}_{-1.1}$	$7.5^{+8.0}_{-4.5} \times 10^{12}$	Y
PLCK_G186.3-72.7-0	1:56:33.074	−18:27:31.60	11.3 ± 1.8	$3.0^{+1.3}_{-1.0}$	$1.3^{+1.7}_{-0.8} \times 10^{13}$	Y
PLCK_G186.3-72.7-1	1:56:33.636	−18:28:47.60	8.7 ± 2.0	$5.2^{+2.4}_{-1.7}$	$1.2^{+1.0}_{-0.6} \times 10^{13}$	Y
PLCK_G186.3-72.7-2	1:56:34.199	−18:28:39.60	8.7 ± 2.0	$2.9^{+1.2}_{-1.0}$	$1.4^{+1.8}_{-0.9} \times 10^{13}$	Y
PLCK_G186.6+66.7-0	11:08:36.022	35:06:04.00	12.7 ± 2.4	$4.8^{+1.8}_{-1.5}$	$1.5^{+1.3}_{-0.8} \times 10^{13}$	Y
PLCK_G188.6-68.9-0	2:11:48.227	−17:00:57.40	13.4 ± 1.9	$2.4^{+1.1}_{-1.0}$	$1.3^{+2.0}_{-1.0} \times 10^{13}$	Y
PLCK_G188.6-68.9-10	2:11:45.159	−17:00:41.40	9.1 ± 2.1	$2.5^{+1.1}_{-1.0}$	$1.1^{+1.6}_{-0.8} \times 10^{13}$	Y
PLCK_G188.6-68.9-11	2:11:52.688	−16:59:01.40	9.9 ± 2.4	$4.2^{+2.2}_{-1.4}$	$9.5^{+9.1}_{-5.3} \times 10^{12}$	Y

Gal ID	RA J2000	Dec J2000	S_{850} (mJy)	$z_{\rm phot}$	Far-IR Luminosity ($L_\odot$)	In Planck Beam
PLCK_G188.6-68.9-1	2:11:49.063	−17:02:49.40	8.8 ± 1.5	$2.5^{+1.0}_{-0.8}$	$8.7^{+10.7}_{-5.3} \times 10^{12}$	Y
PLCK_G188.6-68.9-2	2:11:52.131	−17:02:45.40	8.3 ± 1.5	> 5.1	$1.2^{+1.2}_{-0.6} \times 10^{13}$	Y
PLCK_G188.6-68.9-3	2:11:38.745	−17:01:09.38	10.4 ± 2.0	$2.5^{+1.1}_{-0.9}$	$1.2^{+1.6}_{-0.8} \times 10^{13}$	Y
PLCK_G188.6-68.9-4	2:11:33.720	−17:04:21.36	11.6 ± 2.4	$3.1^{+1.2}_{-1.1}$	$1.4^{+1.5}_{-0.9} \times 10^{13}$	Y
PLCK_G188.6-68.9-5	2:11:44.878	−17:05:57.40	9.2 ± 2.0	$2.6^{+1.0}_{-0.9}$	$9.9^{+11.7}_{-6.6} \times 10^{12}$	N
PLCK_G188.6-68.9-6	2:11:51.853	−17:05:49.40	11.2 ± 2.5	$3.0^{+1.2}_{-1.0}$	$1.7^{+2.1}_{-1.1} \times 10^{13}$	N
PLCK_G188.6-68.9-7	2:11:42.649	−17:00:57.39	8.9 ± 2.0	> 5.7	$1.2^{+1.1}_{-0.6} \times 10^{13}$	Y
PLCK_G188.6-68.9-8	2:11:47.669	−17:01:45.40	7.1 ± 1.6	$3.1^{+1.1}_{-1.0}$	$1.0^{+1.1}_{-0.6} \times 10^{13}$	Y
PLCK_G188.6-68.9-9	2:11:56.315	−17:03:21.39	7.8 ± 1.8	$4.6^{+2.2}_{-1.4}$	$8.8^{+8.0}_{-4.7} \times 10^{12}$	Y
PLCK_G191.3+62.0-0	10:44:57.144	33:51:38.09	12.2 ± 3.0	$1.6^{+0.8}_{-0.7}$	$1.2^{+1.9}_{-0.9} \times 10^{13}$	Y
PLCK_G191.3+62.0-1	10:45:07.096	33:50:50.03	16.0 ± 3.9	$3.3^{+1.3}_{-1.0}$	$1.1^{+1.1}_{-0.6} \times 10^{13}$	Y
PLCK_G191.8-83.4-0	1:18:28.190	−24:34:10.19	9.6 ± 1.6	$4.1^{+1.6}_{-1.4}$	$1.0^{+1.0}_{-0.6} \times 10^{13}$	Y
PLCK_G191.8-83.4-1	1:18:23.791	−24:34:26.17	12.8 ± 2.2	$3.4^{+1.3}_{-1.1}$	$1.4^{+1.6}_{-0.8} \times 10^{13}$	Y
PLCK_G191.8-83.4-2	1:18:21.148	−24:36:42.15	10.9 ± 1.9	$3.2^{+1.3}_{-1.1}$	$1.1^{+1.2}_{-0.7} \times 10^{13}$	Y
PLCK_G191.8-83.4-3	1:18:30.241	−24:35:38.19	9.1 ± 1.6	$3.0^{+1.2}_{-1.0}$	$1.2^{+1.5}_{-0.7} \times 10^{13}$	Y
PLCK_G191.8-83.4-4	1:18:25.253	−24:37:30.17	9.4 ± 1.8	$2.0^{+0.9}_{-0.8}$	$1.2^{+1.8}_{-0.9} \times 10^{13}$	Y
PLCK_G191.8-83.4-5	1:18:39.920	−24:36:10.20	8.7 ± 1.7	$2.1^{+0.9}_{-0.8}$	$9.2^{+11.6}_{-6.4} \times 10^{12}$	Y
PLCK_G191.8-83.4-6	1:18:27.605	−24:32:46.18	8.7 ± 1.9	> 6.2	$1.3^{+1.3}_{-0.6} \times 10^{13}$	Y
PLCK_G191.8-83.4-7	1:18:36.693	−24:34:38.20	6.8 ± 1.5	$2.5^{+1.8}_{-1.0}$	$7.7^{+10.2}_{-5.0} \times 10^{12}$	Y
PLCK_G191.8-83.4-8	1:18:41.680	−24:36:46.19	7.5 ± 1.8	$3.0^{+1.1}_{-1.0}$	$8.7^{+9.5}_{-5.3} \times 10^{12}$	Y
PLCK_G191.8-83.4-9	1:18:36.986	−24:34:42.20	6.0 ± 1.5	$3.5^{+3.3}_{-1.6}$	$6.8^{+7.2}_{-4.0} \times 10^{12}$	Y
PLCK_G201.1+50.7-0	9:53:11.581	27:54:30.40	9.2 ± 1.7	$3.3^{+1.2}_{-1.1}$	$1.1^{+1.2}_{-0.7} \times 10^{13}$	Y
PLCK_G201.1+50.7-1	9:53:08.864	27:55:38.39	8.3 ± 1.8	$1.9^{+1.4}_{-0.8}$	$9.2^{+12.5}_{-6.3} \times 10^{12}$	N
PLCK_G201.1+50.7-2	9:53:14.598	27:56:02.40	7.2 ± 1.6	$3.7^{+1.5}_{-1.2}$	$8.5^{+9.0}_{-5.0} \times 10^{12}$	Y
PLCK_G201.1+50.7-3	9:53:08.562	27:55:34.39	7.6 ± 1.8	$3.0^{+2.5}_{-1.4}$	$8.3^{+9.5}_{-5.4} \times 10^{12}$	N
PLCK_G213.0+65.9-0	11:04:38.213	24:36:35.50	12.3 ± 3.0	$3.6^{+1.3}_{-1.1}$	$1.3^{+1.2}_{-0.7} \times 10^{13}$	Y
PLCK_G213.0+65.9-1	11:04:44.075	24:33:39.48	13.7 ± 3.4	$4.8^{+1.6}_{-1.3}$	$1.5^{+1.2}_{-0.8} \times 10^{13}$	Y
PLCK_G223.9+41.2-0	9:37:14.190	10:00:05.39	16.2 ± 1.9	$2.5^{+1.1}_{-0.9}$	$1.6^{+2.2}_{-1.1} \times 10^{13}$	Y
PLCK_G223.9+41.2-1	9:36:45.214	10:01:45.37	14.0 ± 2.3	$3.2^{+1.2}_{-1.1}$	$1.4^{+1.5}_{-0.9} \times 10^{13}$	N
PLCK_G223.9+41.2-2	9:37:03.088	9:58:25.40	7.2 ± 1.2	$1.2^{+0.7}_{-0.6}$	$6.1^{+12.5}_{-4.7} \times 10^{12}$	Y
PLCK_G223.9+41.2-3	9:36:52.257	9:58:45.39	9.4 ± 1.7	$2.9^{+1.2}_{-1.0}$	$1.2^{+1.4}_{-0.7} \times 10^{13}$	Y
PLCK_G223.9+41.2-4	9:37:18.523	10:00:41.38	12.4 ± 2.4	> 5.6	$1.7^{+1.3}_{-0.8} \times 10^{13}$	Y
PLCK_G223.9+41.2-5	9:37:01.192	9:58:29.40	5.9 ± 1.2	$2.4^{+0.9}_{-0.9}$	$6.3^{+7.6}_{-4.2} \times 10^{12}$	Y
PLCK_G223.9+41.2-6	9:36:42.512	9:56:21.36	10.2 ± 2.3	$4.4^{+2.0}_{-1.4}$	$1.1^{+0.9}_{-0.6} \times 10^{13}$	N
PLCK_G223.9+41.2-7	9:36:50.633	9:58:25.38	7.5 ± 1.8	$4.3^{+1.9}_{-1.4}$	$8.4^{+7.9}_{-4.7} \times 10^{12}$	Y
PLCK_G328.9+71.4-0	13:24:12.114	10:15:42.39	15.5 ± 3.0	$3.4^{+1.3}_{-1.2}$	$1.8^{+2.0}_{-1.1} \times 10^{13}$	N
PLCK_G328.9+71.4-1	13:24:03.171	10:12:22.40	10.5 ± 2.1	$2.2^{+0.9}_{-0.8}$	$1.3^{+1.7}_{-0.9} \times 10^{13}$	Y
PLCK_G328.9+71.4-2	13:23:44.744	10:14:10.37	13.6 ± 3.1	> 6.8	$2.0^{+3.1}_{-0.9} \times 10^{13}$	Y
PLCK_G328.9+71.4-3	13:23:46.372	10:12:22.37	12.9 ± 3.1	> 6.9	$2.0^{+4.6}_{-0.9} \times 10^{13}$	Y